

Design, characterization, and intracellular trafficking of biofunctionalized chitosan nanomicelles

Cite as: *Biointerphases* **15**, 061003 (2020); doi: [10.1116/6.0000380](https://doi.org/10.1116/6.0000380)

Submitted: 8 June 2020 · Accepted: 27 October 2020 ·

Published Online: 13 November 2020



Weiyl Li,¹ Giulia Suarato,^{1,a)} Jillian M. Cathcart,² Paul R. Sargunas,¹ and Yizhi Meng^{1,b)}

AFFILIATIONS

¹Department of Materials Science and Chemical Engineering, Stony Brook University, Stony Brook, New York 11794

²Department of Molecular and Cellular Pharmacology, Stony Brook University, Stony Brook, New York 11794

^{a)}**Present address:** Smart Materials, Group & Translational Pharmacology Facility, Istituto Italiano di Tecnologia, Genova, Italy.

^{b)}**Author to whom correspondence should be addressed:** yizhi.meng@stonybrook.edu

ABSTRACT

The hydrophobically modified glycol chitosan (HGC) nanomicelle has received increasing attention as a promising platform for the delivery of chemotherapeutic drugs. To improve the tumor selectivity of HGC, here an avidin and biotin functionalization strategy was applied. The hydrodynamic diameter of the biotin-avidin-functionalized HGC (cy5.5-HGC-B4F) was observed to be 104.7 nm, and the surface charge was +3.1 mV. Confocal and structured illumination microscopy showed that at 0.1 mg/ml, cy5.5-HGC-B4F nanomicelles were distributed throughout the cytoplasm of MDA-MB-231 breast cancer cells after 2 h of exposure without significant cytotoxicity. To better understand the intracellular fate of the nanomicelles, entrapment studies were performed and demonstrated that some cy5.5-HGC-B4F nanomicelles were capable of escaping endocytic vesicles, likely via the proton sponge effect. Quantitative analysis of the movements of endosomes in living cells revealed that the addition of HGC greatly enhanced the motility of endosomal compartments, and the nanomicelles were transported by early and late endosomes from cell periphery to the perinuclear region. Our results validate the importance of using live-cell imaging to quantitatively assess the dynamics and mechanisms underlying the complex endocytic pathways of nanosized drug carriers.

Published under license by AVS. <https://doi.org/10.1116/6.0000380>

I. INTRODUCTION

The application of nanotechnology in cancer therapy leads to great developments in nanoparticle (NP)-based drug delivery systems for diverse therapeutic agents. In general, NPs are defined as particles with a size range between 1 and 1000 nm in at least one dimension.¹ They can preferentially circulate and accumulate at tumor sites through the enhanced permeation and retention effect caused by the leaky tumor vasculature and defective lymphatic drainage, achieving enhanced tumor targeting and prolonged therapeutic effect.² In recent decades, self-assembling polymeric nanomicelles have been extensively exploited as carriers for poorly water-soluble anticancer drugs.³ Under an aqueous environment, polymeric nanomicelles display a shell-core structure above the critical micelle concentration (CMC), allowing for the solubilization of hydrophobic drugs in the core and the stabilization and protection of the internal reservoir from the surroundings.

Among the various polymeric nanomicelles used for drug delivery, chitosan, a deacetylated derivative of chitin, has attracted much attention due to its nontoxicity, pH sensitivity, biodegradability, and biocompatibility.^{4–6} Glycol chitosan is a commercially available derivative of chitosan with greatly improved water solubility. It can be modified with a hydrophobic bile acid, 5 β -cholanolic acid, to enable the self-assembly of amphiphilic hydrophobically modified glycol chitosan (HGC) nanomicelle. Comprising a hydrophilic shell and a hydrophobic core, HGC has been proven as an efficient carrier for various chemotherapeutic drugs and genes such as paclitaxel, camptothecin, doxorubicin, and siRNA.^{7–11}

In order to improve the therapeutic potential of nanomicelles, it is crucial to understand their intracellular fate. Upon entry into cells via distinct endocytic pathways, incoming nanocarriers may be rapidly recycled to the plasma membrane, and some of them may become trapped in early endosomes (pH 6.1–6.8). Then, early endosomes mature into late endosomes (pH 4.8–6.0) and

subsequently fuse with more acidic lysosomes (pH 4.5).^{12,13} This significant drop in pH in the endocytic pathway leads to the degradation of cargo therapeutics by lysosomal enzymes, which is considered as a critical barrier to the intracellular release of drug payloads.¹⁴ Therefore, it is beneficial to develop nanosized drug carriers that can escape this degradative pathway and efficiently release the therapeutic cargo into the cytosol. Notably, cationic polymers with high buffering capacities over a broad pH range have been shown to escape from endolysosomal compartments via the proton sponge effect and, therefore, are favored for drug delivery applications.^{15–19} The proton sponge hypothesis was first proposed by Bossif in 1995 with an attempt to explain the high transfection efficiency of polyethylenimine.²⁰ The endolysosomal escape of chitosan, the only natural cationic polysaccharide, and its derivatives have been observed in multiple studies.^{21–25} However, due to the lack of direct evidence, the proton sponge effect of chitosan and other cationic polymers remains controversial with many reports questioning its validity.^{26–28} Recently, hypotheses such as the polyplex-mediated membrane disruption and the polymer-mediated membrane disruption have been introduced as alternative endosomal escape mechanisms.^{29–31}

In the present study, HGC was biofunctionalized with a biotin and avidin binding strategy. As one of the strongest noncovalent bonds known in nature, the biotin and avidin interaction is highly specific and can be easily linked to different molecules.³² Here, biotin-4-fluorescein (B4F) was used as a model targeting ligand and was linked to HGC nanomicelles via biotin and avidin binding. The physicochemical properties of the biofunctionalized HGC (cy5.5-HGC-B4F) nanomicelles were characterized, and their intracellular uptake was tracked using *in vitro* confocal studies and structured illumination microscopy (SIM). The endosomal entrapment of the nanomicelles was investigated using SIM, which provided direct evidence in support of the proton sponge model. To better understand the endosomal trafficking of nanomicelles, the intracellular movements of endocytic vesicles in living cells treated with HGC were quantitatively evaluated using high-resolution time-lapse videomicroscopy at the single-cell level. To date, an increasing number of studies have been conducted to investigate endosomal trafficking using live-cell imaging techniques.^{33–37} However, most of these studies focused on local endosomal events that occurred within only a few seconds or minutes and lacked a global understanding of the endocytic process.³⁸ Herein, we described an analytical method with which the movements of endosomal compartments were tracked for hours.

II. MATERIALS AND METHODS

A. Materials

Glycol chitosan (high molecular weight), *N*-hydroxysuccinimide sodium salt (sulfo-NHS), 5 β -cholic acid, and 1-ethyl-3-(3-dimethylaminopropyl) carbodiimide hydrochloride were purchased from Sigma-Aldrich (St. Louis, MO). The 4'-hydroxyazobenzene-2-carboxylic acid/avidin (HABA/avidin) assay kit, sulfo-NHS-LC-biotin, avidin, CellLight Early/Late Endosomes-green fluorescent protein (GFP), wheat germ agglutinin (WGA) conjugated with Texas Red-X, 4',6-diamidino-2-phenylindole dihydrochloride (DAPI), Hoechst 33342 solution, goat antimouse IgG

(H + L) secondary antibody, and Alexa Fluor 488 were purchased from Thermo Fisher Scientific (Rockford, IL). Cyanine5.5 NHS ester (cy5.5 NHS ester) was purchased from Lumiprobe (Hallandale Beach, FL). B4F was obtained from Biotium (Hayward, CA). D-(+)-biotin was purchased from Santa Cruz Biotechnology (Dallas, TX). Serum-free, phenol red-free Dulbecco's modified Eagle medium (DMEM) and Leibovitz's L-15 medium (L-15) were obtained from Gibco (Carlsbad, CA). Mouse anti-EEA1 (clone 14) monoclonal antibody was purchased from BD Biosciences (San Jose, CA).

B. Synthesis of biotin-avidin-functionalized HGC nanomicelles

The detailed preparation process of biotin-avidin-functionalized HGC (cy5.5-HGC-B4F) is described in the supplementary material.⁷⁰ Briefly, glycol chitosan (GC) was biotinylated with sulfo-NHS-LC-biotin to obtain biotinylated glycol chitosan (BGC), followed by linking to avidin (BGCA). The level of biotinylation was quantified by the HABA/avidin assay according to the manufacturer's instructions and was calculated using Eq. (1). Then, 5 β -cholic acid was applied to hydrophobically modify BGCA (BHGCA). After that, B4F was incorporated into BHGCA via the biotin-avidin binding, and cy5.5 NHS ester (cy5.5) was conjugated to the nanomicelles to yield the functionalized nanomicelles (cy5.5-HGC-B4F). Similarly, HGC and biotinylated HGC (BHGC) nanomicelles were prepared, and biotin-avidin-functionalized HGC nanomicelles without fluorescence labeling (HGC-B) were synthesized by linking D-(+)-biotin to BHGCA for cytotoxicity study. To enable the visualization of unmodified nanoparticles, HGC was fluorescently labeled with cy5.5 (cy5.5-HGC) using a method similar to the conjugation of cy5.5 to HGC-B4F and used in the subsequent intracellular trafficking studies,

$$\text{Biotinylation efficiency} = \frac{\text{amount of grafted biotin}}{\text{amount of added biotin}} \times 100\%. \quad (1)$$

C. Characterization of cy5.5-HGC-B4F nanomicelles

The particle size distribution and surface charge of cy5.5-HGC and cy5.5-HGC-B4F were examined using a dynamic light scattering (DLS) and zeta potential system (Malvern Instruments, Westborough, MA, USA). Prior to analysis, the nanomicelles were suspended in HPLC water (0.25 mg/ml), probe-type sonicated (S-450D Sonifier, Branson Ultrasonics, Danbury, CT) at 90 W three times for 2 min in an ice bath and filtered with 0.8 and 0.2 μ m syringe filters. The particle size measurements were taken in backscattering mode, and the surface charge measurements were performed in zeta dip cells. The particle size and surface charge values are expressed as the mean \pm standard deviation.

For transmission electron microscopy (TEM), a small drop (5 μ l) of the nanomicelle suspension was deposited onto 300-mesh copper TEM grids coated with a lacey film and allowed to dry at room temperature in darkness. The TEM images were captured with a JEOL 1400 TEM (JEOL Ltd., Peabody, MA) at an accelerating voltage of 60 keV.

D. MTS assays

MDA-MB-231 human breast carcinoma cells were seeded in 24-well plates at 7500 cells/cm^2 in phenol red-free Dulbecco's Modified Eagle medium (DMEM) containing 4.5 g/l glucose, supplemented with 4 mM L-glutamine, 1% penicillin/streptomycin, and 10% fetal bovine serum (FBS) and allowed to attach at 37°C in a 5% CO_2 atmosphere overnight. The nanomicelles were suspended in phenol red-free DMEM, followed by probe-type sonication and sterile filtration through a $0.2 \mu\text{m}$ syringe filter. Then, the cells were exposed to nonfluorescently labeled HGC, BHGC, or HGC-B suspensions at concentrations ranging from 0.1 to $300 \mu\text{g/ml}$ for up to 72 h. On the day of the assay, fresh cell culture medium was given and the 3-(4,5-dimethylthiazol-2-yl)-5-(3-carboxymethoxyphenyl)-2-(4-sulfophenyl)-2H-tetrazolium (MTS) assay (Promega, Madison, WI) was performed according to the manufacturer's protocol. The absorbance at 490 nm was recorded with a spectrophotometer (Tecan Infinite 200 PRO, Tecan, Switzerland).

E. Cellular uptake

The cellular uptake and intracellular stability of cy5.5-HGC-B4F nanomicelles were investigated in MDA-MB-231 cells. In brief, the cells were seeded at 15000 cells/cm^2 onto 12 mm circular glass coverslips previously placed inside the wells of a 24-well plate and allowed to attach overnight. Then, a $100 \mu\text{g/ml}$ suspension of cy5.5-HGC-B4F in serum-free DMEM was added, and the cells were incubated for up to 24 h. At desired time points, the cells were fixed with 3.7% formaldehyde for 15 min and permeabilized with 0.4% Triton X-100 for 8 min. The cell membranes were stained with Texas Red-X-conjugated WGA ($5 \mu\text{g/ml}$) for 10 min, followed by washing with PBS, and the cell nuclei were stained with DAPI ($2.5 \mu\text{g/ml}$) for 5 min. The glass coverslips were then mounted on microscope slides and imaged with a Zeiss LSM 510 META NLO two-photon confocal laser scanning microscope (CLSM) and a Nikon structured illumination microscope (N-SIM).

F. Entrapment within early endosomes

The MDA-MB-231 cells were seeded at 15000 cells/cm^2 onto 12 mm circular glass coverslips in the wells of a 24-well plate and allowed to attach overnight. Before treatment, the cells were maintained at 4°C for 15 min to preadapt to the low temperature. Then, the cells were treated with a $20 \mu\text{g/ml}$ suspension of cy5.5-HGC or cy5.5-HGC-B4F prepared in cold serum-free DMEM and incubated at 4°C for another 1 h. Cells cultured in serum-free DMEM were served as controls. Subsequently, the cells were washed with ice-cold PBS and transferred to 37°C . At desired time points, the cells were fixed with 3.7% formaldehyde for 15 min and permeabilized with 0.2% Triton X-100 for 7 min. To stain the early endosomes, the fixed cells were first incubated with 5% normal goat serum for 30 min, followed by incubation with mouse antihuman EEA1 primary antibodies at 1:250 dilution for 1 h. Secondary antibodies (Alexa Fluor 488- and rhodamine-conjugated goat antimouse secondary antibodies for cy5.5-HGC- and cy5.5-HGC-B4F-treated cells, respectively) were then applied for 1 h at a dilution of 1:2000, and the cell nuclei were stained with Hoechst 33342 (1:2000) for 5 min. The stained

cells were observed under an N-SIM microscope equipped with a $100\times$ objective (NA 1.30).

G. Time-lapse videomicroscopy

Endosomal trafficking in living MDA-MB-231 cells treated with cy5.5-HGC was monitored by time-lapse fluorescence microscopy. Specifically, the MDA-MB-231 cells were seeded in 35 mm glass-bottom MatTek dishes ($150000 \text{ cells/dish}$) and allowed to attach overnight. Subsequently, $75 \mu\text{l}$ of CellLight early or late endosome-GFP reagent was added to label either the early endosomal or late endosomal vesicles in the cells and further incubated for 24 h. Prior to imaging, the cells were washed with PBS and replaced with fresh phenol red-free Leibovitz's-15 (L-15) medium supplemented with 10% FBS and 1% penicillin/streptomycin to maintain the physiological pH. A cy5.5-HGC suspension was added to the cells at a final concentration of 0.2 mg/ml , and the cells were visualized immediately using an Olympus IX51 inverted fluorescence microscope equipped with a $60\times$ objective at 37°C in the absence of CO_2 . The time-lapse images were acquired up to 180 min at 1-min intervals from 0 to 4 min, at 2-min intervals from 4 to 20 min, at 5-min intervals from 20 to 120 min, and at 10-min intervals from 120 to 180 min. Cells cultured in only complete L-15 medium were also imaged and served as controls.

H. Image analysis

The time-lapse images were analyzed using IMAGEJ software with the Manual Tracking plug-in [Ref. 39](#). More than 40 early and late endosomes from each MDA-MB-231 cell were randomly selected for image processing. The velocity and distance traveled by each early and late endosome were measured based on the pixel coordinates (1 pixel = $0.107 \mu\text{m}$).

III. RESULTS

A. Biotinylation and avidinylation of glycol chitosan

As shown in [Fig. 1\(a\)](#), BGC was prepared by reacting the amino groups on the GC backbone with sulfo-NHS-LC-biotin. The biotinylation level of BGC was determined using the HABA/avidin assay and the absorbance of HABA/avidin and BGC mixture was recorded at 500 nm. According to the HABA/avidin assay, 24.29 mol of biotin molecules were successfully conjugated to 1 mol of GC and available for binding to avidin, rendering a biotinylation efficiency of 97.93%. After the biotinylation process, avidin was linked to BGC to form biotinylated and avidinylated glycol chitosan (BGCA). For BGCA containing both biotin and avidin, the biotinylation level was decreased to $14.10 \text{ mol biotin/mol BGCA}$. This indicates that only 14 biotin molecules remained available for binding after the avidinylation process, revealing that on average the added avidin connected to 10 biotins on each BGC molecule. With four identical subunits, each avidin molecule can accommodate a maximum of four biotinylated moieties; therefore, at an avidin:BGC feed ratio of 3:1 (mol/mol), for every BGC molecule, 12 biotin-binding sites were presented. Out of these 12 binding sites, 10 became occupied by avidin, leaving 2 empty binding sites available for subsequent binding with B4F. Following the

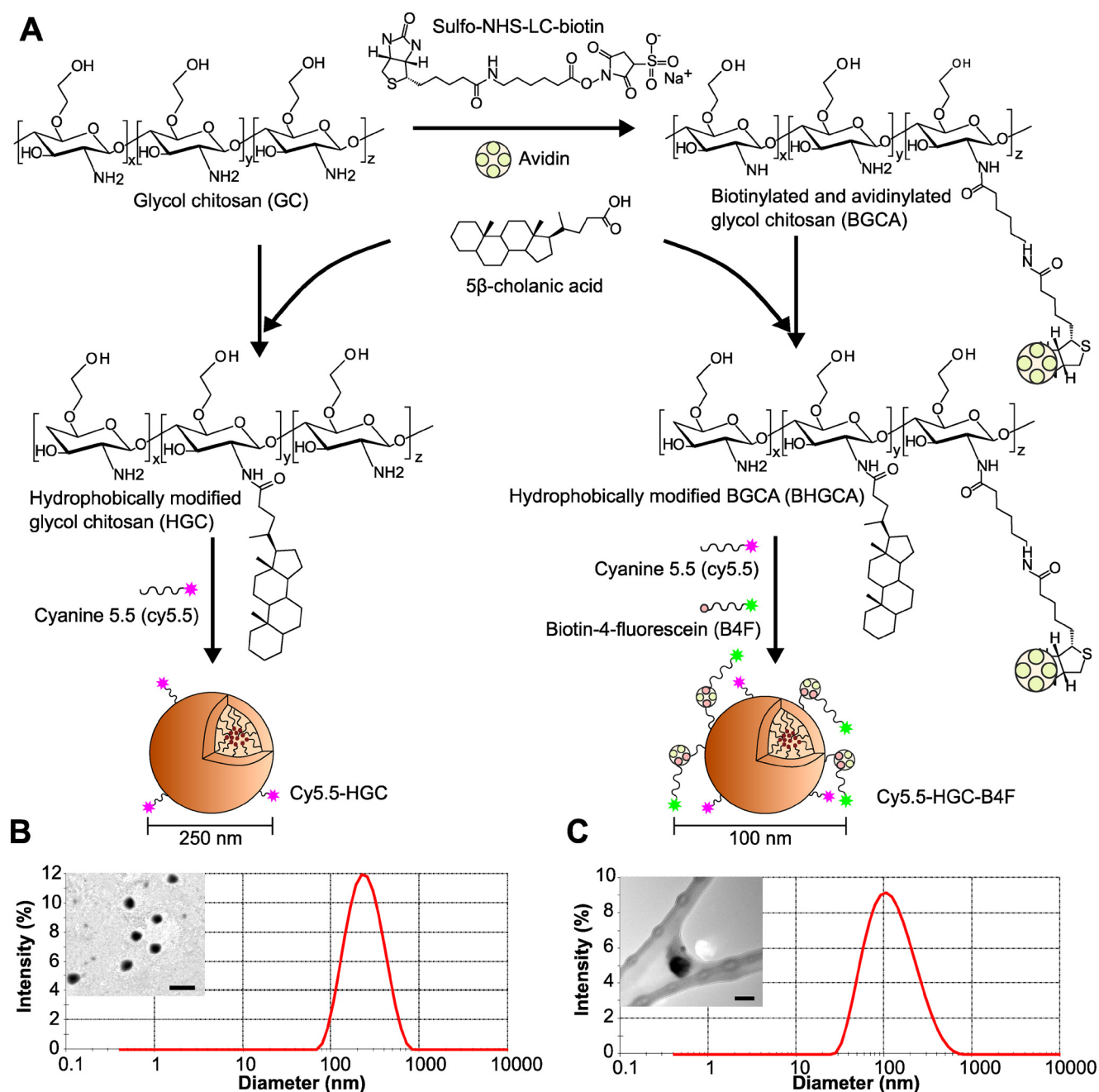


FIG. 1. (a) Synthesis scheme of cy5.5-labeled hydrophobically modified glycol chitosan (cy5.5-HGC) and biotin-avidin-functionalized HGC (cy5.5-HGC-B4F). (b) Dynamic light scattering analysis of cy5.5-HGC nanomicelles. Inset: TEM image showing individual cy5.5-HGC micelles. Scale bar, 500 nm. (c) Dynamic light scattering analysis of cy5.5-HGC-B4F nanomicelles. Inset: TEM image showing a single cy5.5-HGC-B4F micelle. Scale bar, 100 nm.

avidinylation process, 5 β -cholanolic acid was attached to the free amino groups on BGCA to facilitate the self-assembly of hydrophobically modified BGCA (BHGCA) nanomicelles. The degree of substitution (DS), defined as the number of 5 β -cholanolic acid per

100 sugar residues of GC, was estimated to be 18.5. Subsequently, cy5.5 NHS ester was conjugated to the amino group of GC, and B4F was attached to the nanomicelles by binding to avidin. Based on the above calculations, it was estimated that in the resultant

biotin-avidin-functionalized HGC (cy5.5-HGC-B4F) nanomicelle, B4F was linked to BHGCA at a molar ratio close to 2:1.

B. Physical characteristics of cy5.5-HGC-B4F nanomicelles

The hydrodynamic diameters (z-average) of cy5.5-HGC and cy5.5-HGC-B4F nanomicelles were determined by DLS to be 269.2 ± 7.1 and 104.7 ± 4.1 nm, respectively [Figs. 1(b) and 1(c)]. The corresponding polydispersity values were 0.20 and 0.25, respectively, indicating a narrow range of particle size distribution of cy5.5-HGC and cy5.5-HGC-B4F nanomicelles. Moreover, the TEM images reveal the spherical morphologies of cy5.5-HGC and cy5.5-HGC-B4F, with size ranges of 230–250 and 80–100 nm, respectively [inset of Figs. 1(b) and 1(c)]. The slightly decreased particle size of both nanomicelles noted in the TEM images as compared to that in the DLS measurements was most likely due to the drying process of the TEM grid preparation. The surface charges of the cy5.5-HGC and cy5.5-HGC-B4F nanomicelles were measured to be $+16.0 \pm 0.6$ and $+3.1 \pm 0.7$ mV, respectively, which can be explained by the cationic nature of chitosan.

C. In vitro cytotoxicity studies

To assess the effects of biotinylation and avidinylation on the biocompatibility of HGC nanomicelles, we analyzed the cytotoxicity of nonfluorescently labeled HGC, BHGC, and biotinylated and avidinylated HGC (HGC-B) in the MDA-MB-231 cells (Fig. 2). The percentage cell viability was defined as the ratio of the absorbance of treated cells to that of untreated cells. Noticeably, the viability of cells treated with either HGC or BHGC was maintained at or above 80% for up to 72 h, at all concentrations tested [Figs. 2(a) and 2(b)]. In contrast, nanomicelles that were further avidinylated (HGC-B) caused significant cell death after 72 h of exposure at 300 μ g/ml ($p < 0.001$), as the viability of cells dropped to 19.3% [Fig. 2(c)], demonstrating the enhanced cytotoxic activity of the nanomicelles upon surface modification by avidin. It is interesting to note that when HGC-B was applied at concentrations lower than 300 μ g/ml, cell viability remained above 80%. Thus, cy5.5-HGC-B4F at concentrations below 300 μ g/ml was used for the following cellular uptake studies to ensure the full viability of the cells.

D. Cellular uptake of cy5.5-HGC-B4F nanomicelles

To examine the cellular uptake and distribution of the nanomicelles, the MDA-MB-231 cells treated with 100 μ g/ml cy5.5-HGC-B4F were evaluated using CLSM. In the CLSM images, avidin-bound B4F was visualized in the green channel, whereas cy5.5-conjugated HGC was visualized in the magenta channel [Fig. 3(a)]. After 2 h of incubation, colocalization (visualized as white regions) between B4F and cy5.5 was observed throughout the cytoplasm. Pearson's correlation coefficient (PCC) analysis ($n = 4$) was performed for the colocalization of B4F and cy5.5 using IMAGEJ software with the Coloc 2 plug-in [Fig. 3(c)].⁴⁰ The PCC values greater than 0.6 indicated a quite high degree of colocalization of B4F and cy5.5 in the cytoplasm. To further understand the intracellular distribution of nanomicelles, the cells were visualized using N-SIM [Fig. 3(b)]. By overcoming the resolution limit of

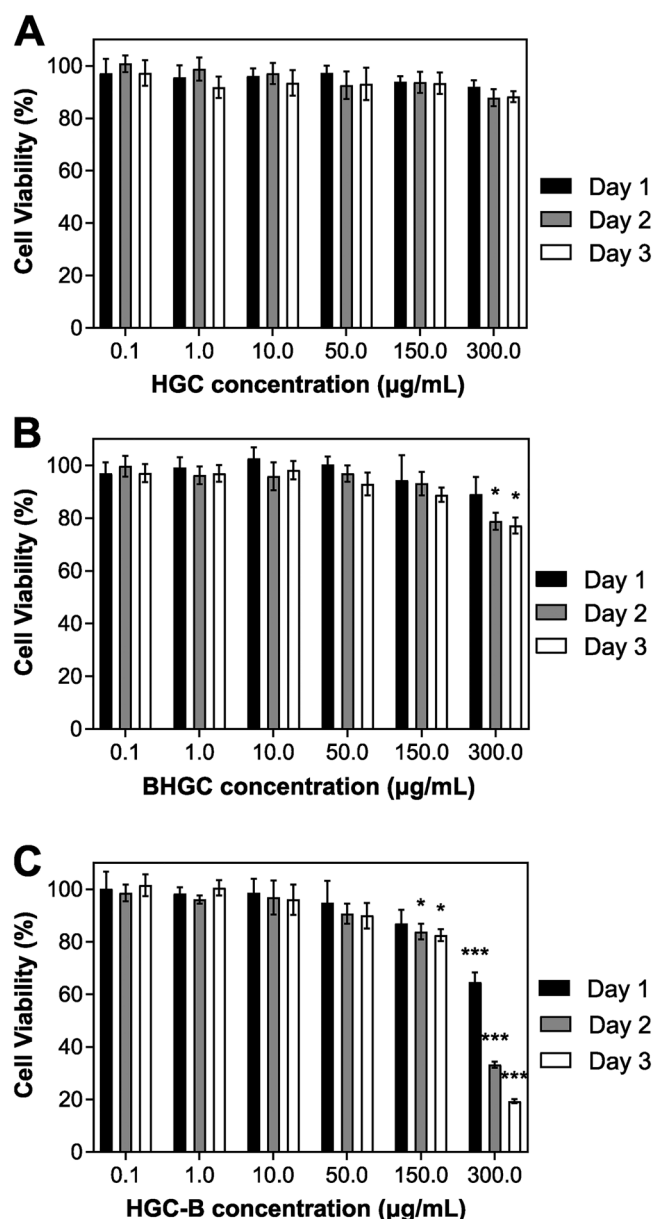


FIG. 2. Cell viability of MDA-MB-231 cells treated with (a) HGC, (b) BHGC, or (c) HGC-B for up to 3 days. All data are presented as the mean \pm standard deviation from three independent experiments. The viability of treated cells was compared to that of untreated cells, * $p < 0.05$ significant, ** $p < 0.01$ very significant, and *** $p < 0.001$ extremely significant.

conventional microscopes, N-SIM allows for the observation of individual nanosized particles. The cell plasma membrane was visualized by Texas Red-X-conjugated WGA staining. In accordance with the CLSM images, the N-SIM images also reveal clear colocalization between B4F and cy5.5, as evidenced by individual white spots throughout the cytoplasm. In addition, the

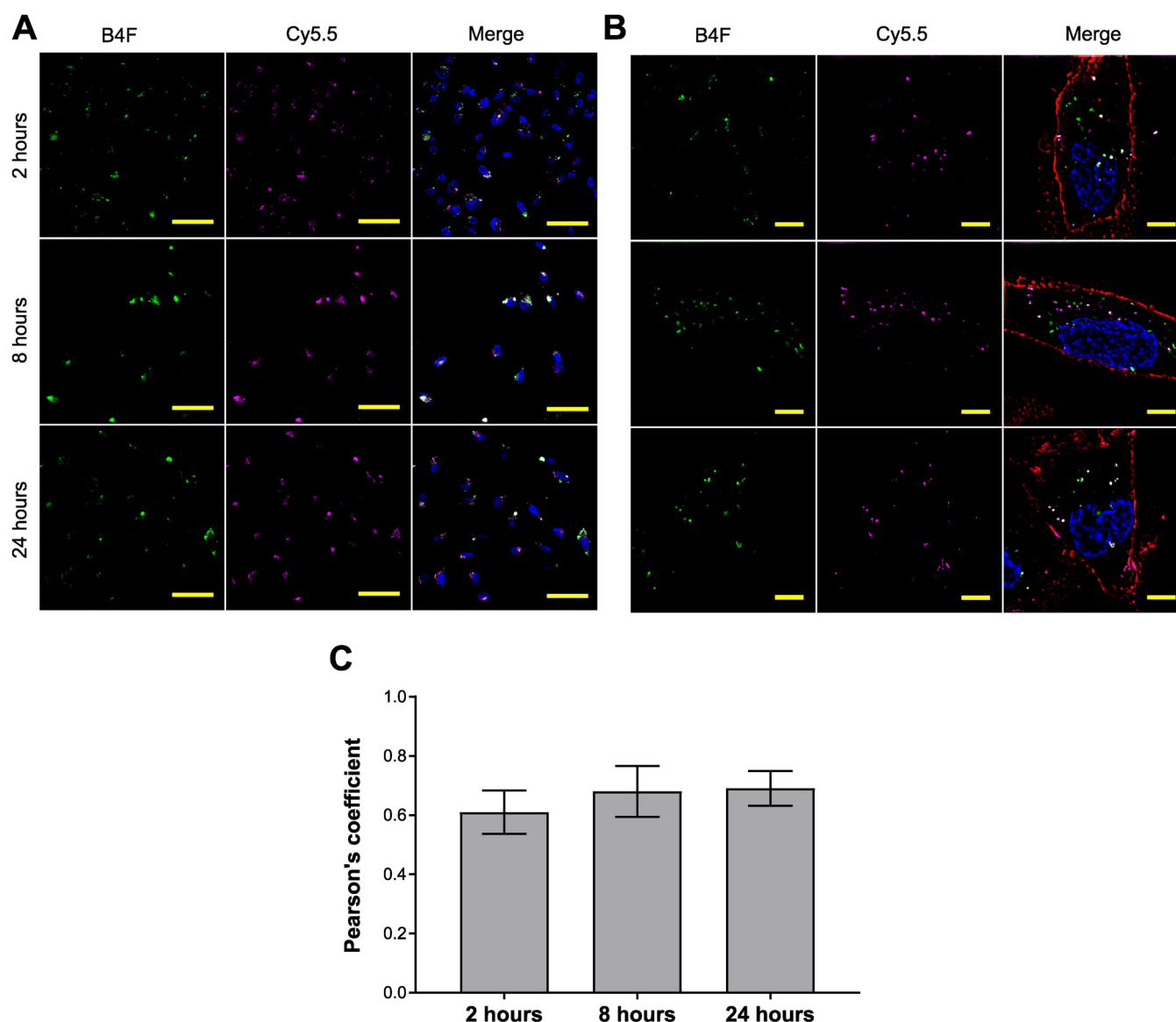


FIG. 3. Cellular uptake of cy5.5-HGC-B4F nanomicelles visualized by (a) CLSM and (b) N-SIM. B4F is visualized in the green channel, and cy5.5 is visualized in the magenta channel. The cell nuclei were stained with DAPI (blue) and cell membranes were stained with Texas-Red-labeled WGA (red). Scale bar, (a) 50 μm and (b) 5 μm . (c) Analysis of fluorescence colocalization. Pearson's correlation coefficient \pm standard deviation ($n = 4$) for the colocalization of cy5.5 and B4F in the CLSM images was obtained with IMAGEJ.

nanomicelles were observed to distribute within the cells without any colocalization with the plasma membrane over the course of the entire experiment, suggesting that cy5.5-HGC-B4F nanomicelles were internalized by the cells within 2 h of incubation.

E. Entrapment of nanomicelles within early endosomes

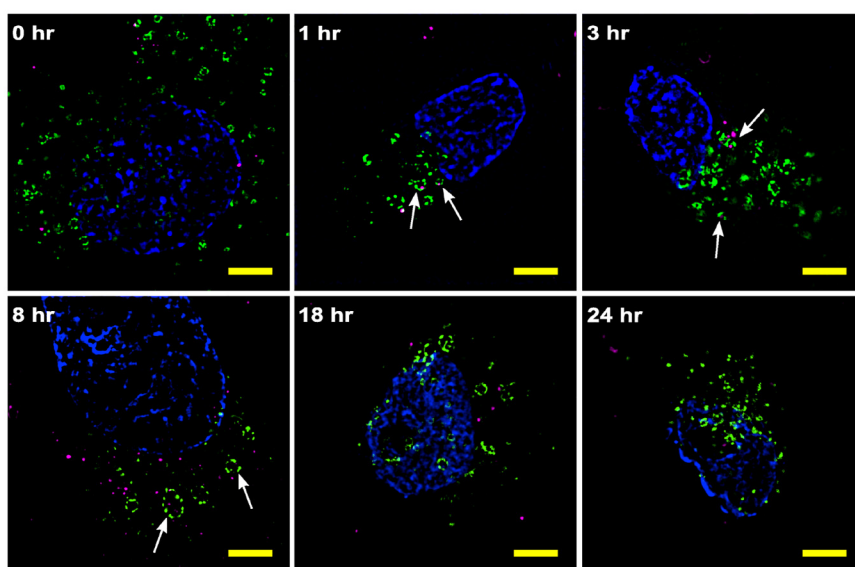
The intracellular fate of nanomicelles was examined in MDA-MB-231 cells after a 1-h incubation with 20 $\mu\text{g}/\text{ml}$

cy5.5-HGC or cy5.5-HGC-B4F initially at 4 $^{\circ}\text{C}$, which would block endocytosis due to the temperature sensitivity of several proteins and enzymes.^{41,42} Afterwards, the endocytotic processes were allowed to resume at 37 $^{\circ}\text{C}$ for the desired time points. In the N-SIM images, cy5.5-HGC and cy5.5-HGC-B4F nanomicelles appear as magenta dots, and the early endosomes stained with anti-EEA1 antibody are pseudocolored green. According to Fig. 4(a), at 1–8 h postincubation at 37 $^{\circ}\text{C}$, cy5.5-HGC nanomicelles were present both around and within the circular endosomal

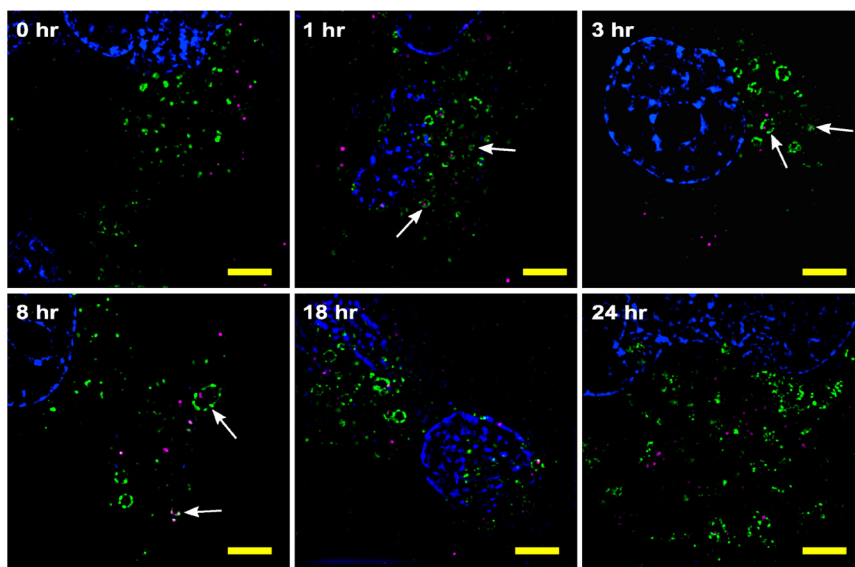
structures, as indicated by the white arrows. As reported in Video S1 in the supplementary material,⁷⁰ the 3D reconstruction of the z-stack clearly reveals the entrapment of nanomicelles in the early endosomes at 3 h postincubation. At time points longer than 8 h (i.e., 18 and 24 h), the nanomicelles were no longer entrapped

within the early endosomes [Fig. 4(a)]. The average diameter of early endosomes and the percentage of cy5.5-HGC nanomicelles entrapped in the early endosomes were measured across 6 cells per time point using IMAGEJ software [see Figs. 5(a) and 5(b)]. Interestingly, when treated with cy5.5-HGC, at time 0, the early

A



B



C

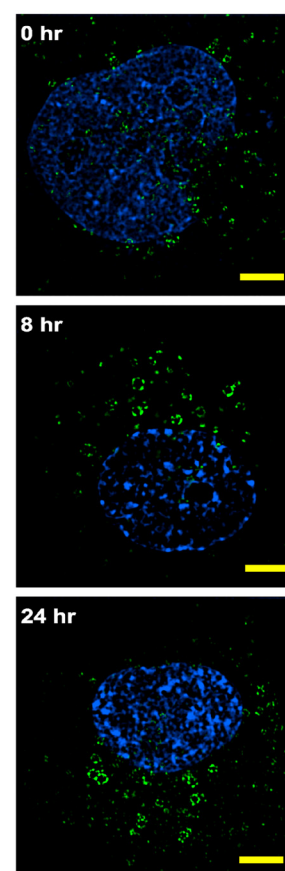


FIG. 4. N-SIM images of MDA-MB-231 cells treated with (a) cy5.5-HGC (magenta) and (b) cy5.5-HGC-B4F (magenta). (c) Early endosomes in untreated cells. The early endosomal vesicles were visualized by immunofluorescence staining with anti-EEA1 monoclonal antibodies (pseudocolored green). The cell nuclei were stained with Hoechst (blue). The white arrows indicate the entrapment of nanomicelles in the early endosomes. Scale bar, 5 μ m.

endosomes appeared as small circular structures (747.3–789.8 nm in diameter). As the incubation time increased, a greater fraction of HGC nanomicelles was entrapped in the early endosomes [Fig. 5(b)], while the early endosomes gradually increased in size [Figs. 4(a) and 5(a), filled circle]. After reaching a maximum size at 8 h (1265.7–1332.5 nm in diameter), the early endosomes started to shrink and the ratio of entrapped nanomicelles decreased. The enlargement of early endosomes could be associated with the fusion events between early endosomes, the maturation of early endosomes, as well as the accumulation of nanomicelles.^{12,37} Similar trends of nanomicelle entrapment and endosomal enlargement from 1 to 8 h postincubation were observed in cy5.5-HGC-B4F-treated cells [Figs. 4(b), 5(a), and 5(b), empty triangle]. On the contrary, in untreated cells [Fig. 4(c)], no significant change in early endosomal diameter could be detected at 0, 8, or 24 h [$p > 0.05$, Fig. 5(c), empty square]. The size of early endosomes observed in this study is consistent with a previous report in which early endosomes displayed a tubulovesicular structure with a diameter up to 1000 nm.⁴³

F. Live-cell trafficking of early and late endosomes in human breast cancer cells

To explore the exact route of intracellular tracking, herein, living MDA-MB-231 cells transfected to express GFP-tagged marker proteins for either early (Rab5) or late (Rab7) endosomes were examined by time-lapse videomicroscopy at 37 °C. As shown in Fig. 6, at time 0 (immediately after exposure to nanomicelles), both early and late endosomes located in the periphery of the cell appeared as small round structures (Fig. 6, yellow arrows), while a few larger endosomes were found in the perinuclear region (Fig. 6, yellow arrowheads). Following the addition of cy5.5-HGC, endosomes at the cell periphery underwent saltatory oscillations, with a net directional movement toward the nucleus [Figs. 7(a) and 7(b)]. Endosomes that were initially close to the nucleus migrated in random directions over a short distance and remained near the nucleus. On the contrary, early and late endosomes in untreated cells moved back and forth in a restricted region, exhibiting what was likely to be Brownian motion [Figs. 7(c) and 7(d)]. The time-lapse videos are shown in Videos S2, S3, S4, and S5 in the supplementary material.⁷⁰ Quantitative analysis of the trajectories of early and late endosomes revealed that the motility of both early and late endosomes was considerably enhanced by the addition of nanomicelles, as evidenced by the significant increase in the velocity and the distance [$p < 0.001$, Figs. 8(a) and 8(b)].

Endosome velocity was further plotted as a function of incubation time [Figs. 8(c) and 8(d)]. In untreated cells, the velocities of early endosomes [Fig. 8(c)] and late endosomes [Fig. 8(d)] fluctuated with a slight decrease with time, indicating that endosomes are dynamic motile structures. In comparison, early and late endosomes in cells treated with cy5.5-HGC exhibited significantly high velocities ($p < 0.001$) at all time points. Surprisingly, the velocity of early endosomes displayed an overall, steady decrease [Fig. 8(c)], while the late endosomes showed alternating slow and fast movements, reaching a peak velocity of 12.66 $\mu\text{m}/\text{h}$ between 100 and 110 min [Fig. 8(d)]. This peak indicated that the maturation of early endosomes into late endosomes or the fusion of late

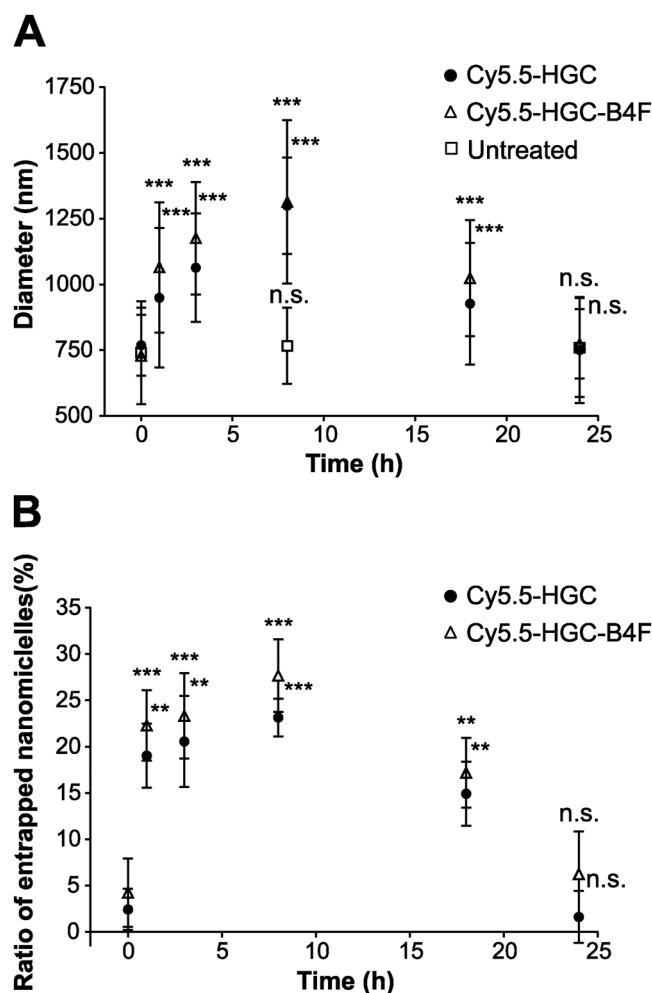


FIG. 5. (a) Quantitative analysis of early endosome size in MDA-MB-231 cells treated with cy5.5-HGC or cy5.5-HGC-B4F nanomicelles. The early endosomal diameters of treated cells and untreated cells at each time point were compared to the corresponding diameters at 0 h. (b) Ratio of nanomicelles entrapped in the early endosomes to total nanomicelles within the cells treated with cy5.5-HGC or cy5.5-HGC-B4F nanomicelles. The % nanomicelle entrapment at each time point was compared to that at 0 h. All data are presented as the mean \pm standard deviation of two independent experiments, n.s.: not significant, * $p < 0.05$ significant, ** $p < 0.01$ very significant, and *** $p < 0.001$ extremely significant.

endosomes with lysosomes was most apparent between 100 and 110 min.

IV. DISCUSSION

In this study, we present an approach with which HGC is bio-conjugated to a model targeting ligand, B4F, using an avidin-biotin-binding strategy. Due to the easy linkage of ligands, this functionalization strategy has been proven to be a versatile tool

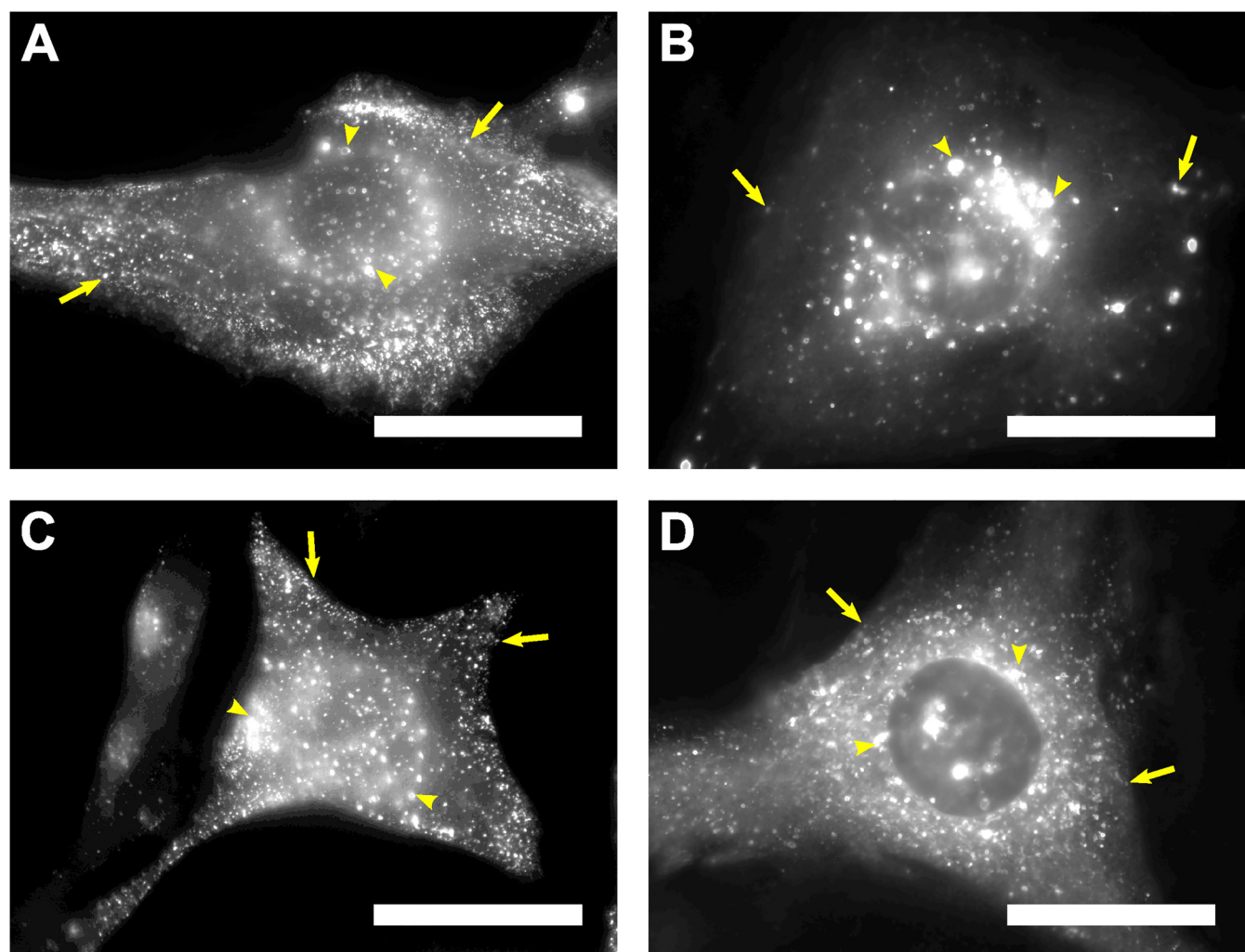


FIG. 6. Spatial distribution of (a) EE and (b) LE in MDA-MB-231 cells treated with cy5.5-HGC, and (c) EE and (d) LE in untreated cells at 0 min. The yellow arrows indicate the endosomes located in the cell periphery and the yellow arrowheads indicate the endosomes in the perinuclear region. Scale bar, 50 μ m.

for preparing multifunctional nanocarriers for different site-specific drug delivery applications.^{44,45} The complete biofunctionalized nanomicelles (cy5.5-HGC-B4F) displayed an average diameter of 104.7 ± 4.1 nm with a surface charge of $+3.1 \pm 0.7$ mV. Nanocarriers with diameters larger than 200 nm are more likely to be captured by phagocytic cells in the reticuloendothelial system and small nanoparticles (<5 nm) will be rapidly cleared by renal filtration.^{46–48} Thus, cy5.5-HGC-B4F nanomicelles with a diameter of about 100 nm are expected to attain an extended circulation time upon intravenous injection. In comparison, the average diameter and zeta potential of cy5.5-HGC nanomicelles without the avidin and biotin functionalization were found to be 269.2 ± 7.1 nm and $+16.0 \pm 0.6$ mV, respectively. The differences in diameters and surface charges of cy5.5-HGC and cy5.5-HGC-B4F are consequences of the biofunctionalization of HGC. More

specifically, the decreased amount of GC molecules per nanomicelle with the addition of biotin, avidin, and B4F molecule might result in a reduction in nanomicelle size. This observation is in agreement with a previous study in which nanoparticles shrank due to a decreased amount of chitosan in chitosan/DNA nanoparticles.³² Moreover, the relatively lower content of GC in cy5.5-HGC-B4F resulted in the increased molar ratio hydrophobic 5β -cholanolic acid to hydrophilic GC and, therefore, facilitated the formation of more hydrophobic and more compact nanomicelles than nonavidin-biotin-modified HGC.⁴⁹ The lower zeta potential observed for cy5.5-HGC-B4F, compared to that for cy5.5-HGC, may be attributed to the conjugation of sulfo-NHS-LC-biotin molecules to GC. Based on the results from the HABA/avidin assay, about 24 sulfo-NHS-LC-biotin molecules were successfully conjugated to each GC molecule, during which the conversion of

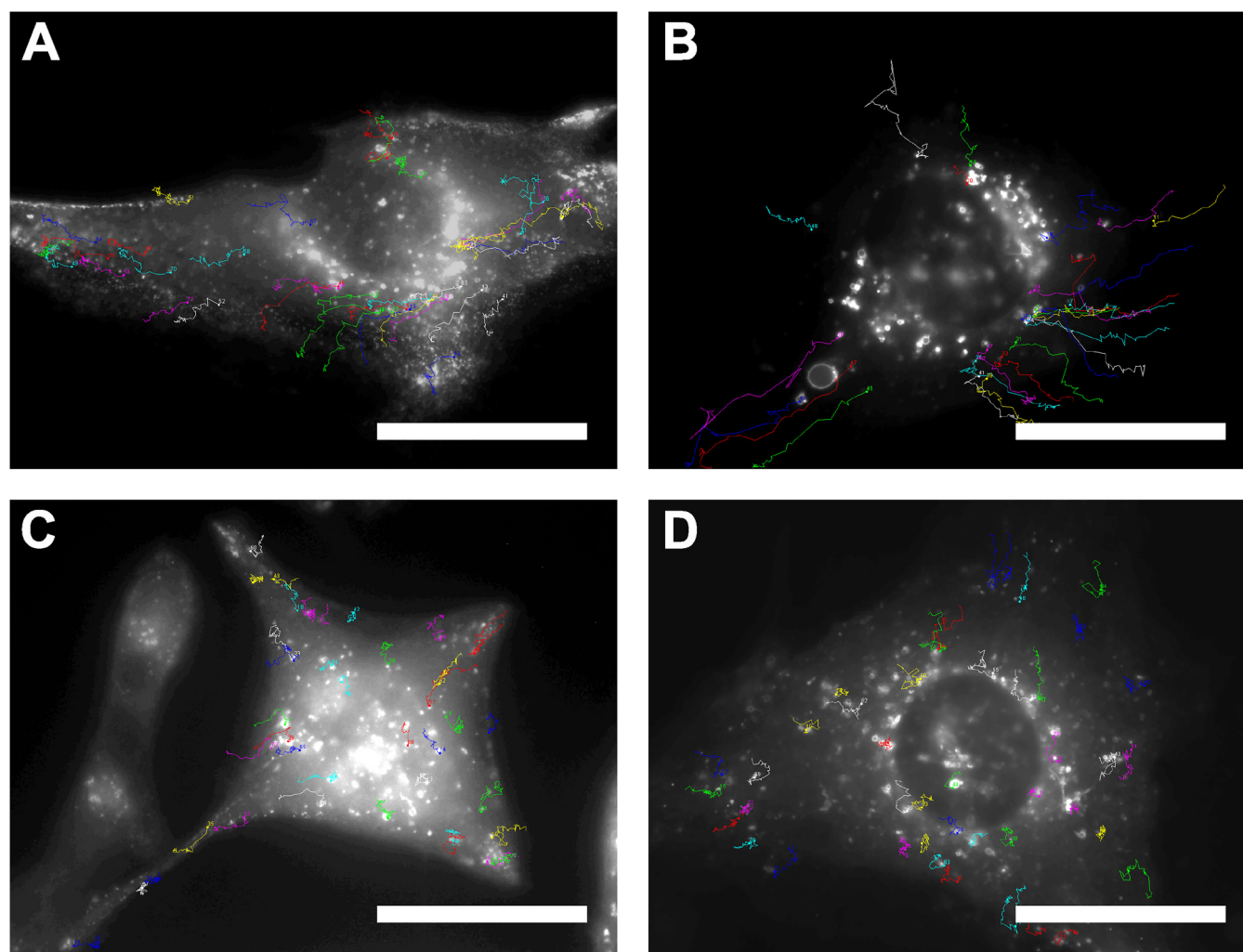


FIG. 7. Representative tracks of movements and spatial distribution of (a) EE and (b) LE in MDA-MB-231 cells treated the cy5.5-HGC, and (c) EE and (d) LE in untreated cells at 180 min. Scale bar, 50 μ m.

positively charged amino groups to amide linkages could lead to an overall reduction in the positive surface charge.

Biotin, also known as vitamin H, plays an important role in assisting various metabolic reactions related to amino acids and carbohydrates and hence is expected to be nontoxic. Avidin is a glycoprotein found in egg whites and its safety and biocompatibility have been proved in clinical trials.⁵⁰ Although avidin, biotin, and GC are generally considered to be safe, the linkage of biotin and avidin to HGC might lead to potential toxicity. Thus, the cytotoxic effects of HGC and functionalized HGC were assessed (Fig. 2). Compared to unmodified HGC, BHGC demonstrated similar cytotoxic activity, indicating that the biotinylation process indeed did not negatively affect the metabolic activity of cells. However, surface modification by avidin enhanced the cytotoxic capacity of the nanomicelles at the delivered concentration of

300 μ g/ml. Avidin has been reported to bind to lectins expressed on the surface of tumor cells that develop peritoneal metastases.^{51,52} Therefore, nanomicelles biofunctionalized with avidin could be recognized by lectins on the surface of breast cancer cells, and subsequently internalized into the cells, probably leading to enhanced cellular uptake and subsequent cytotoxicity. This result correlates with a previous study, where avidinylated and biotinylated chitosan nanoparticles showed much more potent cytotoxicity against HepG2 cells than biotinylated chitosan nanoparticles.⁵³

Based on the CLSM and N-SIM images, at a delivered concentration of 100 μ g/ml, cy5.5-HGC-B4F nanomicelles were taken up by MDA-MB-231 cells within 2 h and were dispersed widely throughout the cytoplasm for up to 24 h. The observed colocalization of B4F and cy5.5 at all time points indicated the successful linkage between B4F and HGC and suggested that the

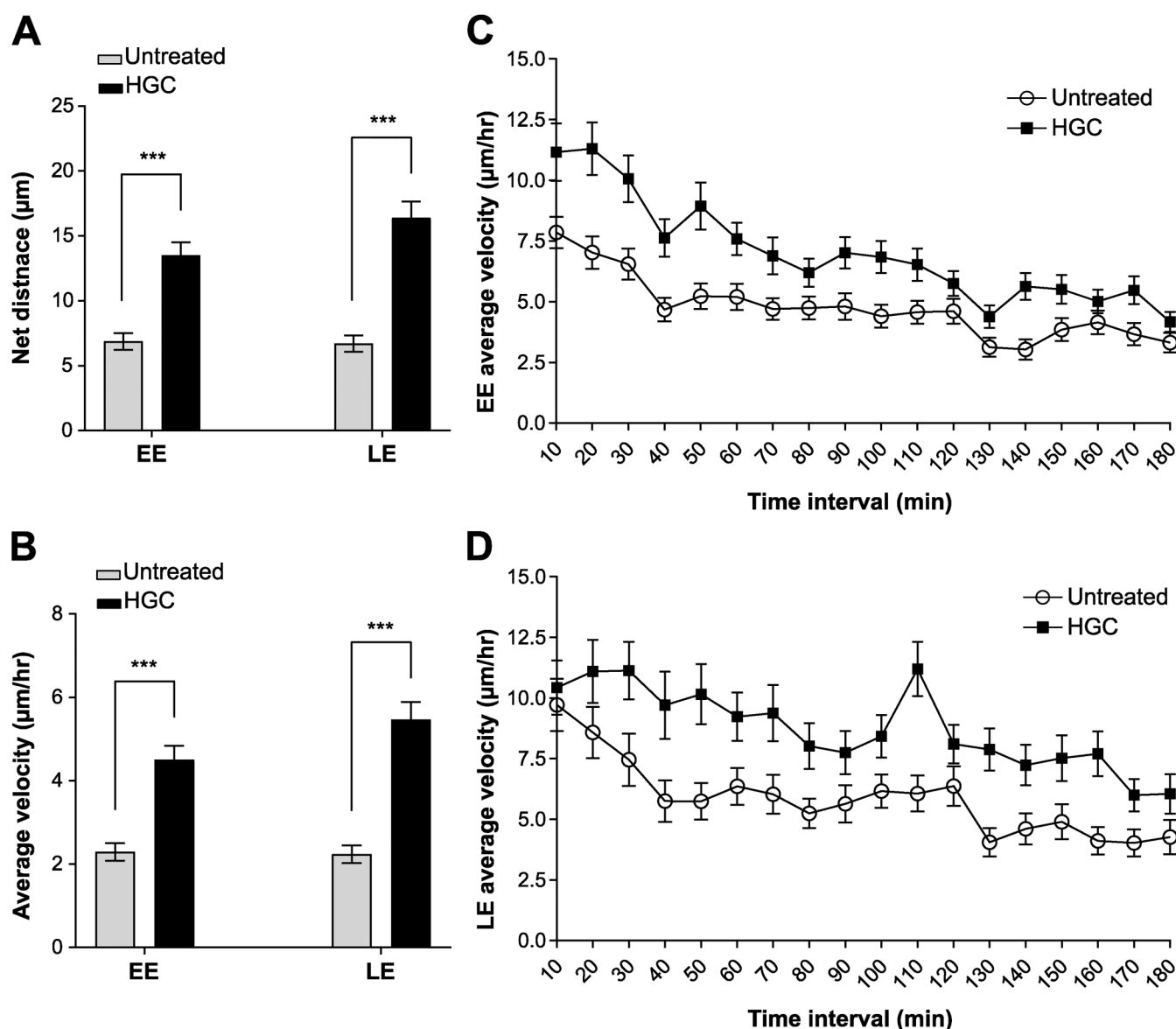


FIG. 8. (a) Net distances and (b) average velocities of EE and LE in MDA-MB-231 cells from 0 to 180 min after the addition of cy5.5-HGC. The average velocities of (c) EE and (d) LE in MDA-MB-231 cells within every 10 min after the addition of cy5.5-HGC. All data are presented as the mean \pm SEM (standard error of the mean) (N = four cells in four independent experiments), *** $p < 0.001$ extremely significant.

biofunctionalized nanomicelles were stable in the intracellular environment. The stability of cy5.5-HGC-B4F could be attributed to the strong avidin-biotin bond known to be stable over a wide range of pH and temperature.⁵⁴ In addition, the N-SIM images revealed the rapid cellular uptake of biofunctionalized HGC nanomicelles by MDA-MB-231 cells within 2 h of incubation, which was probably facilitated by the electrostatic interactions between the cationic cy5.5-HGC-B4F with the negatively charged plasma membrane of cells.⁵⁵

Understanding intracellular fate and transport is critical for the design of an efficient drug delivery platform. Generally, following uptake, nanocarriers are transported from early endosomes to late endosomes and lysosomes, with a significant drop in pH.⁵⁶ The acidic environment can disrupt chemical bonds and distort particle structure, resulting in the rapid release of the therapeutic cargo. Recently, super-resolution microscopy has been proposed as a powerful tool to image particle-cell interactions and intracellular trafficking of nanoparticles with subdiffraction resolution.^{18,57–60} In

the current study, the endosomal trafficking of cy5.5-HGC and cy5.5-HGC-B4F possessing a smaller size and a less positive surface charge compared to nonavidin-biotin-modified HGC was exploited using N-SIM combined with quantitative image analysis. According to Figs. 4 and 5, the clear entrapment of cy5.5-HGC nanomicelles within individual early endosomes from 1 to 8 h post-incubation and the accompanying swelling of early endosomes were visualized with nanometric resolution. Subsequently, less entrapment was observed, and the early endosomes shrank to their original size after 24 h. Consistently, when the cells were treated with cy5.5-HGC-B4F, the early endosomes swelled in size with increased nanomicelle entrapment from 1 to 8 h and shrank from 18 to 24 h postincubation. The enlargement of early endosomes induced by the administration of cy5.5-HGC (269.2 nm, +16.0 mV) and cy5.5-HGC-B4F (104.7 nm, +3.1 mV) nanomicelles with different sizes and surface charges could be credited to the high buffering capacity of chitosan.⁶¹ In contrast, the early endosomes in untreated cells remained the same size from 0 to 24 h postincubation. Taken together, these results support the proton sponge model, which suggests that upon entry of nonavidin-biotin-modified or modified HGC into the cells, the membrane-bound ATPase proton pumps acidify the early endosomes by transporting protons from the cytosol into the early endosomes. Once cationic HGC is entrapped within early endosomes at 1 h postincubation, the amines on HGC likely become protonated under this acidic condition to resist the acidification of early endosomes, and hence more protons are continuously pumped into the early endosomes to lower the pH. The pumping of protons is compensated by the passive entry of chloride ions (Cl^-). The accumulation of Cl^- in the early endosomes eventually leads to an influx of water from the cytosol and ultimately results in osmotic swelling and rupture of the endosomal membrane, followed by the release of nanomicelles into the cytosol after 18 h postincubation. In contrast, the other two possible theories of endosomal escape, polyplex-mediated membrane disruption and polymer-mediated membrane disruption, do not suggest the swelling of endosomal compartments and, therefore, may be unsuitable to explain the escape behavior of HGC nanomicelles in MDA-MB-231 cells.^{29,30}

Because the immunofluorescence staining was performed after the cells were fixed, we next examined the fate of nanomicelles in a living cell. As illustrated in Fig. 7, the early and late endosomes in MDA-MB-231 cells treated with cy5.5-HGC exhibited a centripetal movement from the cell periphery toward the perinuclear region. The centripetal movement of endosomes is known to be mediated by motor proteins such as kinesins and dynein bidirectionally along microtubules and is considered as a sign of endosomal maturation.^{12,62} During this process, nanomicelles internalized from the plasma membrane were trapped and transported by endosomes from the cell periphery to the vicinity of lysosomes in the perinuclear area, which might affect the interaction of endosomes and motor proteins and result in the high motility of endosomal vesicles. Conversely, the observed short-range Brownian-like motion of endosomes in untreated cells elucidated that early and late endosomes are highly dynamic and motile compartments.

In general, early endosomes, as the first sorting compartment, accept incoming cargo for only about 5–10 min, after which they translocate and stop fusing with newly endocytosed vesicles.⁶³ Late

endosomes that are derived from early endosomes through maturation, on the other hand, form in the peripheral cytoplasm and move to the perinuclear area to fuse with each other and with lysosomes, providing the last sorting station in the endocytic pathway.^{64,65} Our results demonstrated that during the first 10 min of incubation with nanomicelles, early endosomes in MDA-MB-231 cells traveled over a long distance of 1.89 μm [Fig. 8(c)], indicating that the nanomicelles might be trapped in early endosomes immediately after internalization and then transported from early endosomes to late endosomes. Unlike early endosomes, late endosomes in MDA-MB-231 cells treated with nanomicelles displayed a discontinuous pattern of movement with overall higher motility [Fig. 8(d)]. Similar findings have been observed in root hairs of Arabidopsis seedlings, in which late endosomes exhibited discontinuous but slower movements compared to early endosomes.³⁶ The motility of endosomes is reported to be regulated by different small GTPase proteins, Rab5 and Rab7,^{66,67} leading to distinct motility profiles. In our study, the late endosomes in nanomicelle-treated cells showed a spike in motility between 100 and 110 min postincubation. This sudden acceleration may be related to the sorting of endocytic cargo (i.e., cy5.5-HGC) from early to late endosomes during endosomal maturation or the fusion of late endosomes with lysosomes. In spite of the fact that the roles of early and late endosomes in the endocytic pathways have been well-defined, the endosomal compartments are complex, dynamic, and unstable, as trapped materials are transported in and out of the compartments through transport vesicles and the endosomal compartments are constantly undergoing maturation in the periphery, in transit, or in the perinuclear region.^{12,63,68} Accordingly, both the entrapment and transportation of cy5.5-HGC nanomicelles in early and late endosomes could occur at the same time. Similarly, along with endosomal trafficking, the maturation of early endosomes to late endosomes or the fusion of late endosomes with lysosomes may have occurred and their motility likely reached a plateau of 12.66 $\mu\text{m}/\text{h}$ from 100 to 110 min after the initial exposure to cy5.5-HGC. Although the proton sponge model offers a reasonable explanation for the early endosomal escape behavior of HGC, we note that late endosomes are actively involved in the endocytic pathways of cy5.5-HGC nanomicelles in MDA-MB-231 cells, as evidenced by our live-cell imaging data. It is possible that a fraction of HGC nanomicelles were able to escape the early endosomes, while others were shuttled to late endosomes and/or lysosomes. Consistently, in HeLa cells, some HGC nanomicelles were found in late endosomes and lysosomes, and some were dispersed in the cytosol upon entry.⁶⁹ Altogether, the endocytic trafficking of HGC could be summarized as follows: (1) HGC nanomicelles were first received and transported by early endosomes immediately after internalization; (2) some of the nanomicelles facilitated early endosomal escape while others were fused into late endosomes and transported from the cell periphery to the perinuclear regions. Further research will be needed to conclusively address the intracellular trafficking behavior of HGC nanomicelles.

In conclusion, we have proposed a versatile and simple bio-functionalization strategy for HGC nanomicelles. The biotin-avidin-functionalized HGC shows enhanced cytotoxic activity upon the surface modification of avidin and is rapidly taken up by MDA-MB-231 breast cancer cells. In addition, the nanomicelle

entrapment studies on fixed cells using N-SIM show that both nonavidin-biotin-modified and modified HGC nanomicelles undergo endosomal escape via the proton sponge effect, as evidenced by the swelling (i.e., at 1–8 h postincubation) and the subsequent shrinkage (i.e., at 18–24 h postincubation) of the early endosomes in cy5.5-HGC- and cy5.5-HGC-B4F-treated cells. The time-lapse videomicroscopy performed on single living cells further demonstrates that cy5.5-HGC nanomicelles are first received by early endosomes after internalization and that the intracellular transportation of HGC is coregulated by early endosomes, late endosomes, and the maturation and fusion events between endosomal and lysosomal compartments. Live-cell imaging techniques allow the direct visualization of the centripetal movements of early and late endosomes and will be a powerful tool for studying drug delivery trafficking and understanding how endocytic pathways can influence the efficiency of drug delivery systems.

NOMENCLATURE

BGC	biotinylated glycol chitosan
BGCA	biotinylated and avidinylated glycol chitosan
BHGC	biotinylated HGC
BHGC	hydrophobically modify BGCA
B4F	biotin-4-fluorescein
CLSM	confocal laser scanning microscopy
cy5.5	cyanine5.5 NHS ester
cy5.5-HGC-B4F	biotin-avidin-functionalized HGC
DAPI	4',6-diamidino-2-phenylindole dihydrochloride
DLS	dynamic light scattering
EDC	1-ethyl-3-(3-dimethylaminopropyl) carbodiimide hydrochloride
EPR	enhanced permeability and retention
FBS	fetal bovine serum
GC	glycol chitosan
GFP	green fluorescent protein
HABA	4'-hydroxyazobenzene-2-carboxylic acid
HGC	hydrophobically modified glycol chitosan
MMP	matrix metalloproteinase
MTS	3-(4,5-dimethylthiazol-2-yl)-5-(3-carboxymethoxyphenyl)-2-(4-sulfophenyl)-2H-tetrazolium
RES	reticuloendothelial system
SIM	structured illumination microscopy
sulfo-NHS	N-hydroxysuccinimide sodium salt
TEM	transmission electron microscopy
WGA	wheat germ agglutinin

ACKNOWLEDGMENTS

The authors sincerely thank Shu Jia and Haoyu Li from the Department of Biomedical Engineering for their assistance with the SIM studies and gratefully acknowledge Deborah Brown from the Department of Biochemistry at Stony Brook University for reading the manuscript. Research reported in this publication was supported by the National Heart, Lung, and Blood Institute of the National Institutes of Health under Award No. U01HL127522. The content is solely the responsibility of the authors and does not necessarily represent the official views of the National Institutes of Health.

Additional support was provided by the Center for Biotechnology, a New York State Center for Advanced Technology, Stony Brook University, Cold Spring Harbor Laboratory, Brookhaven National Laboratory, and Northwell Health.

REFERENCES

- 1 M. Ferrari, *Nat. Rev. Cancer* **5**, 161 (2005).
- 2 K. Greish, in *Cancer Nanotechnology* (Springer, New York, 2010), pp. 25–37.
- 3 G. Suarato, W. Li, and Y. Meng, *Biointerphases* **11**, 04B201 (2016).
- 4 R. Riva, H. Ragelle, A. des Rieux, N. Duhem, C. Jérôme, and V. Préat, in *Chitosan for Biomaterials II* (Springer, New York, 2011), pp. 19–44.
- 5 T. Kean and M. Thanou, *Adv. Drug Deliv. Rev.* **62**, 3 (2010).
- 6 J. P. Quiñones, H. Peniche, and C. Peniche, *Polymers* **10**, 235 (2018).
- 7 J.-H. Kim *et al.*, *J. Control. Release* **111**, 228 (2006).
- 8 K. H. Min *et al.*, *J. Control. Release* **127**, 208 (2008).
- 9 J. H. Park *et al.*, *Biomaterials* **27**, 119 (2006).
- 10 H. Y. Yoon *et al.*, *Sci. Rep.* **4**, 6878 (2014).
- 11 M. Agirre, J. Zarate, E. Ojeda, G. Puras, J. Desbrieres, and J. Pedraz, *Polymers* **6**, 1727 (2014).
- 12 J. Huotari and A. Helenius, *EMBO J.* **30**, 3481 (2011).
- 13 S. D. Conner and S. L. Schmid, *Nature* **422**, 37 (2003).
- 14 P. Sandin, L. W. Fitzpatrick, J. C. Simpson, and K. A. Dawson, *ACS Nano* **6**, 1513 (2012).
- 15 J. Haensler and F. C. Szoka, Jr., *Bioconjug. Chem.* **4**, 372 (1993).
- 16 P. van de Wetering, E. E. Moret, N. M. Schuurmans-Nieuwenbroek, M. J. van Steenberg, and W. E. Hennink, *Bioconjug. Chem.* **10**, 589 (1999).
- 17 N. D. Sonawane, F. C. Szoka, and A. Verkman, *J. Biol. Chem.* **278**, 44826 (2003).
- 18 M. Wojnilowicz, A. Glab, A. Bertucci, F. Caruso, and F. Cavalieri, *ACS Nano* **13**, 187 (2018).
- 19 W. Liang and J. K. Lam, in *Molecular Regulation of Endocytosis* (InTech, Rijeka, Croatia, 2012), pp. 429–456.
- 20 O. Boussif, F. Lezoualc'h, M. A. Zanta, M. D. Mergny, D. Scherman, B. Demeneix, and J.-P. Behr, *Proc. Natl. Acad. Sci. U.S.A.* **92**, 7297 (1995).
- 21 H. Ragelle, G. Vandermeulen, and V. Préat, *J. Control. Release* **172**, 207 (2013).
- 22 P. Sun, W. Huang, L. Kang, M. Jin, B. Fan, H. Jin, Q.-M. Wang, and Z. Gao, *Int. J. Nanomed.* **12**, 3221 (2017).
- 23 K.-L. Chang, Y. Higuchi, S. Kawakami, F. Yamashita, and M. Hashida, *Bioconjug. Chem.* **21**, 1087 (2010).
- 24 H. Lu, Y. Dai, L. Lv, and H. Zhao, *PLoS One* **9**, e84703 (2014).
- 25 Z. Chen *et al.*, *Biomaterials* **52**, 240 (2015).
- 26 Y.-Y. Won, R. Sharma, and S. F. Konieczny, *J. Control. Release* **139**, 88 (2009).
- 27 L. M. Vermeulen, S. C. De Smedt, K. Remaut, and K. Braeckmans, *Eur. J. Pharm. Biopharm.* **129**, 184 (2018).
- 28 R. V. Benjaminsen, M. A. Mattheij, J. R. Henriksen, S. M. Moghimi, and T. L. Andresen, *Mol. Ther.* **21**, 149 (2013).
- 29 Z. U. Rehman, D. Hoekstra, and I. S. Zuhorn, *ACS Nano* **7**, 3767 (2013).
- 30 S. Vaidyanathan, B. G. Orr, and M. M. Banaszak Holl, *Acc. Chem. Res.* **49**, 1486 (2016).
- 31 T. Bus, A. Traeger, and U. S. Schubert, *J. Mater. Chem. B* **6**, 6904 (2018).
- 32 W.-W. Hu, W.-J. Syu, W.-Y. Chen, R.-C. Ruaan, Y.-C. Cheng, C.-C. Chien, C. L. C.-A. Chung, and C.-W. Tsao, *Bioconjug. Chem.* **23**, 1587 (2012).
- 33 P. Watson, A. T. Jones, and D. J. Stephens, *Adv. Drug Deliv. Rev.* **57**, 43 (2005).
- 34 A. Das, S. Nag, A. B. Mason, and M. M. Barroso, *J. Cell Biol.* **214**, 831 (2016).
- 35 A. E. Vasdekis, E. A. Scott, C. P. O'Neil, D. Psaltis, and J. A. Hubbell, *ACS Nano* **6**, 7850 (2012).
- 36 D. von Wangenheim, A. Rosero, G. Komis, O. Šamajová, M. Ovečka, B. Voigt, and J. Šamaj, *Front. Plant Sci.* **6**, 1262 (2016).

- ³⁷F. M. Skjeldal, S. Strunze, T. Bergeland, E. Walseng, T. F. Gregers, and O. Bakke, *J. Cell Sci.* **125**, 1910 (2012).
- ³⁸H. Li, Z.-W. Duan, P. Xie, Y.-R. Liu, W.-C. Wang, S.-X. Dou, and P.-Y. Wang, *PLoS One* **7**, e45465 (2012).
- ³⁹F. Cordelieres, "Manual tracking," 2005, see <https://imagej.nih.gov/ij/plugins/track/track.html>.
- ⁴⁰J. Schindelin, J. Eglinger, L. Guizzetti, M. Hiners, and J.-Y. Tinevez, "Coloc 2," 2017, see https://imagej.net/Coloc_2.
- ⁴¹T. Dos Santos, J. Varela, I. Lynch, A. Salvati, and K. A. Dawson, *PLoS One* **6**, e24438 (2011).
- ⁴²A. L. Munn, *Biochim. Biophys. Acta Mol. Basis Dis.* **1535**, 236 (2001).
- ⁴³S. Ali, *Cell Organisation and Function* (Pearson Education, New Delhi, India, 2014).
- ⁴⁴G. Suarato, S.-I. Lee, W. Li, S. Rao, T. Khan, Y. Meng, and M. Shelly, *Biomaterials* **112**, 176 (2017).
- ⁴⁵W. Yin, W. Li, D. A. Rubenstein, and Y. Meng, *Biointerphases* **11**, 04B301 (2016).
- ⁴⁶S. M. Sadat, S. T. Jahan, and A. Haddadi, *J. Biomater. Nanobiotechnol.* **7**, 91 (2016).
- ⁴⁷E. Blanco, H. Shen, and M. Ferrari, *Nat. Biotechnol.* **33**, 941 (2015).
- ⁴⁸H. Kobayashi, R. Watanabe, and P. L. Choyke, *Theranostics* **4**, 81 (2014).
- ⁴⁹S. Kwon, J. H. Park, H. Chung, I. C. Kwon, S. Y. Jeong, and I.-S. Kim, *Langmuir* **19**, 10188 (2003).
- ⁵⁰G. Paganelli *et al.*, *Cancer Biother. Radiopharm.* **16**, 227 (2001).
- ⁵¹Y. Hama, Y. Urano, Y. Koyama, P. L. Choyke, and H. Kobayashi, *Biochem. Biophys. Res. Commun.* **348**, 807 (2006).
- ⁵²Y. Mine, *Egg Bioscience and Biotechnology* (Wiley, New York, 2008).
- ⁵³L. Bu, L.-C. Gan, X.-Q. Guo, F.-Z. Chen, Q. Song, X.-J. Gou, S.-X. Hou, and Q. Yao, *Int. J. Pharm.* **452**, 355 (2013).
- ⁵⁴E. A. Bayer, H. Ben-Hur, G. Gitlin, and M. Wilchek, *J. Biochem. Biophys. Meth.* **13**, 103 (1986).
- ⁵⁵E. Fröhlich, *Int. J. Nanomed.* **7**, 5577 (2012).
- ⁵⁶S. Mukherjee and F. R. Maxfield, *Nat. Cell Biol.* **1**, E37 (1999).
- ⁵⁷D. van der Zwaag, N. Vanparijs, S. Wijnands, R. De Rycke, B. G. De Geest, and L. Albertazzi, *ACS Appl. Mater. Interfaces* **8**, 6391 (2016).
- ⁵⁸H. Li *et al.*, *Biomed. Opt. Express* **10**, 29 (2019).
- ⁵⁹D. Li *et al.*, *Science* **349**, aab3500 (2015).
- ⁶⁰A. M. Sydor, K. J. Czymmek, E. M. Puchner, and V. Mennella, *Trends Cell Biol.* **25**, 730 (2015).
- ⁶¹I. Richard, M. Thibault, G. De Crescenzo, M. D. Buschmann, and M. Lavertu, *Biomacromolecules* **14**, 1732 (2013).
- ⁶²J. S. Bonifacio and J. Neefjes, *Curr. Opin. Cell Biol.* **47**, 1 (2017).
- ⁶³F. R. Maxfield and T. E. McGraw, *Nat. Rev. Mol. Cell Biol.* **5**, 121 (2004).
- ⁶⁴J. P. Luzio, P. R. Pryor, and N. A. Bright, *Nat. Rev. Mol. Cell Biol.* **8**, 622 (2007).
- ⁶⁵W. Stoorvogel, G. J. Strous, H. J. Geuze, V. Oorschot, and A. L. Schwartz, *Cell* **65**, 417 (1991).
- ⁶⁶C. Lebrand, M. Corti, H. Goodson, P. Cosson, V. Cavalli, N. Mayran, J. Fauré, and J. Gruenberg, *EMBO J.* **21**, 1289 (2002).
- ⁶⁷E. Nielsen, F. Severin, J. M. Backer, A. A. Hyman, and M. Zerial, *Nat. Cell Biol.* **1**, 376 (1999).
- ⁶⁸J. Rink, E. Ghigo, Y. Kalaidzidis, and M. Zerial, *Cell* **122**, 735 (2005).
- ⁶⁹H. Y. Nam *et al.*, *J. Control. Release* **135**, 259 (2009).
- ⁷⁰See supplementary material at <http://dx.doi.org/10.1116/6.0000380> for preparation of biofunctionalized nanomicelles; volume view of the nanomicelle entrapment; live-cell imaging of early and late endosomes in cy5.5-HGC-treated cells; and live-cell imaging of early and late endosomes in untreated cells.